Available online at www.sciencedirect.com
SCIENCE DIRECT®
International Journal of Multiphase Flow 32 (2006) 739–753
International Journal of Multiphase Flow
www.elsevier.com/locate/ijmulflow

# Numerical simulation of fluid–particle hydrodynamics in a rectangular spouted vessel

P.A. Shirvanian *, J.M. Calo, G. Hradil

*Division of Engineering, Brown University, Providence, RI 02912, United States*

Received 15 December 2005; received in revised form 14 February 2006

**Abstract**

A three-dimensional, Eulerian simulation was developed to describe isothermal, two-phase flow of the continuous (water) and dispersed (solid particles) phases in a rectangular spouted vessel. The mass and momentum conservation equations for each phase were solved using the finite volume technique, which treats each phase separately, while coupling them through drag, turbulence, and energy dissipation due to particle fluctuations. Particle–particle interactions *via* friction were also included.

Model results in terms of fluid and solid flow properties, such as volume fraction, pressure and velocity fields were validated with experimental results obtained in a rectangular spouted vessel apparatus. The effects of inlet jet velocity, particle loading, particle diameter, and density on solids volume fraction distributions, pressure field, and particle recirculation rate were investigated with the resultant model. The model is shown to be able to successfully predict the experimentally observed phenomenon of particle "choking" where the particle recirculation rate remains constant with increasing particle loading once a "critical loading" is achieved. Simulations also confirmed the manner in which particle size, density, loading, and inlet jet velocity affect solids circulation.

This investigation was motivated by the need for hydrodynamic information related to the development of spouted bed electrolytic reactors (SBER) as moving bed cathodes for metals recovery.


*Keywords:* Eulerian–Eulerian model; Spouted beds; Particle–particle interactions

## 1. Introduction

The current work is based on applications of liquid-spouted beds of electrically conductive particles as cathodes for electrolytic recovery of metal ions from aqueous solutions (Shirvanian and Calo, 2005). As shown in Fig. 1, in a spouted bed electrolytic reactor (SBER), metal ions are reduced on the surfaces of the circulating, conductive particles when they are resident in the moving bed cathode located on the conical bottom of the spouted vessel. The metal ion-containing solution is introduced as a high velocity liquid jet at the center of the conical bottom of the vessel. The liquid jet entrains particles from the moving bed that move centripetally

* Corresponding author.

0301-9322/$ - see front matter © 2006 Published by Elsevier Ltd.
doi:10.1016/j.ijmultiphaseflow.2006.02.009

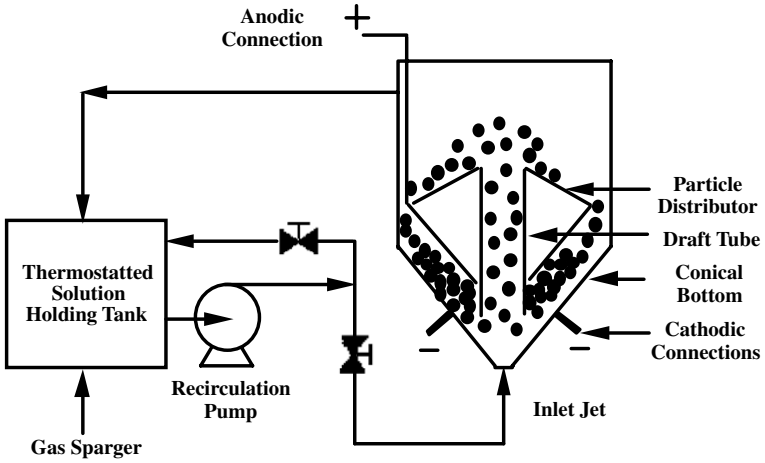


Fig. 1. Schematic of spouted bed electrolytic reactor (SBER) apparatus and flow system for metals recovery.

towards the entrainment point on the conical bottom. The entrained particles disengage from the liquid flow in the ''fountain,'' as they slow down, and fall onto the distributor that directs them to the periphery of the bed where they then fall by gravity onto the moving bed cathode where they are re-directed back to the liquid jet for re-entrainment. The ''pumping action'' provided by the spout circulates the particles in a toroidal fashion through the vessel; upwards in the spout and downwards in the moving bed, as shown in Fig. 1. The residence time distribution of the particles in the moving bed cathode and the particle recirculation rate are important parameters in determining the performance of the SBER.

In comparison to other fluid–solid reactor/contactor types, relatively little has been published on spouted beds. Mathur and Epstein (1974) treated gas–solid spouted beds, operated without a draft tube, using a one-dimensional integral approach. Littman et al. (1979) used a semi-empirical approach to predict maximum spoutable bed height, and developed an expression relating the overall spout pressure drop at minimum spouting to the overall pressure drop at minimum fluidization conditions, in a spouted bed operated with a draft tube. Morgan et al. (1985) used one-dimensional mass and momentum balances for the liquid and solid phases to find the voidage distribution and particle circulation rate in a water-spouted bed with a draft tube.

One of the potential disadvantages of using spouted beds as reactors for certain applications is the relatively broad fluid residence time distribution due to mixing, caused in part by the partitioning of fluid between the spout and the peripheral bed region. This is one of the reasons for employing a draft tube. Morgan et al. (1988) developed empirical expressions for predicting maximum jet penetration depth and pressure drop in a water-spouted bed of fine particles, operated with a draft tube. It was noted that the maximum spoutable bed height and separation distance between the inlet opening and the draft tube entrance are important design parameters.

Subsequently, Matthew et al. (1988) used two-dimensional versions of the Darcy and Ergun equations to describe the hydrodynamics in the draft tube and the peripheral annulus of a spouted bed. From this work, it can be concluded that stable and homogeneous particle circulation can be obtained only over a relatively narrow range of inlet jet velocities that depends on the design of the draft tube. It was also noted that draft tube-spouted beds eliminate the bubbling problem in gas–particle systems, which makes them more attractive as contacting devices. The dynamic behavior of a gas–solid spouted bed was predicted by Lefroy and Davidson (1969) using one-dimensional particle and momentum balances in the spout. Kalwar and Raghavan (1992) used a two-dimensional gas-spouted bed that was geometrically similar to the system investigated in the current work, and investigated the spout pressure drop and minimum spouting superficial velocity. It was concluded that the spout pressure drop increases as the entrainment zone height and the angle of inclination increase, and decreases as the spout width increases. Their observation that the minimum spouting velocity increases with the entrainment length is consistent with the results presented for the rectangular spouted vessel in the experimental studies of Shirvanian and Calo (submitted for publication).

Marschall and Mleczko (1999) performed a numerical investigation of a draft tube gas-spouted bed of very fine (200 μm) particles. These workers investigated the effects of inlet jet velocity on the pressure drop in the draft tube, particle residence time, and void fraction distribution along the axis of the draft tube. A simplified Eulerian approach was used wherein the interaction between phases was modeled with an empirical correlation. Huilin et al. (2001) also used an Eulerian method wherein the constitutive equations describing the particulate solids pressure, viscosity and elasticity moduli were implemented in a hydrodynamic simulation model. The fluid volume fraction distribution and particle and gas velocity distributions across the spouted bed were examined, and reasonably good agreement was obtained between their results and experimental data.

In the current work, a kinetic theory approach for granular flow is used that allows the determination of the pressure and viscosity of the solids phase in lieu of empirical correlations. This approach uses a single expression for granular temperature, assumes a Maxwellian distribution for the particles, and considers both dilute and dense phases, as employed by Kalwar and Raghavan (1992) and Hattori et al. (1998). Interactions between the liquid and solid phases are incorporated in the form of a drag force that is discussed further below.

## 2. Fluid dynamics model

A "two-fluid" (fluid and solid phases), Eulerian–Eulerian model was developed to simulate the hydrodynamics of a rectangular spouted bed, operated with draft duct. Following the approach of workers such as Chapman and Cowling (1990), Ding and Gidaspow (1990), Jenkins and Savage (1983), and Savage and Jeffrey (1981), the solid-phase stresses are based on an analogy between the random particle motion arising from particle–particle collisions and the thermal motion of molecules in a gas, taking into account the inelasticity of the granular phase. The intensity of the particle velocity fluctuations determines the stresses, viscosity, and pressure of the solid phase. The kinetic energy associated with the particle velocity fluctuations is represented by a "pseudothermal" or granular temperature that is proportional to the mean square of the random motion of the particles.

### 2.1. Model summary

Syamlal et al. (1993), Drew and Passman (1999), Drew (1983), and Enwald et al. (1996) used spatial, time, and ensemble averages in developing the equations of motion for two-phase flow systems. Assuming no interphase mass transfer, the continuity equations for the liquid and particulate phase ($q = s$ for solid, and $f$ for fluid/liquid) are:

$$\frac{\partial}{\partial t}\alpha_q\rho_q + \nabla\cdot\alpha_q\rho_q\vec{u}_q = 0, \tag{1}$$

where $t$, $\alpha_q$, $\rho_q$ and $\vec{u}_q$ are time, volume fraction, averaged density, and averaged velocity vector associated with phase $q$, respectively. The volume fraction of the solid and liquid are related through the constraint, $\alpha_s + \alpha_f = 1$. The momentum conservation equations for the liquid and solid phases are given by the following expressions:

$$\frac{\partial}{\partial t}(\alpha_f\rho_f\vec{u}_f) + \nabla\cdot(\alpha_f\rho_f\vec{u}_f\otimes\vec{u}_f) = -\alpha_f\nabla p + \nabla\cdot\overline{\overline{\tau}}_f + \alpha_f\rho_f\vec{g} + K_{sf}(\vec{u}_s - \vec{u}_f), \tag{2}$$

$$\frac{\partial}{\partial t}(\alpha_s\rho_s\vec{u}_s) + \nabla\cdot(\alpha_s\rho_s\vec{u}_s\otimes\vec{u}_s) = -\alpha_s\nabla p - \nabla p_s + \nabla\cdot\overline{\overline{\tau}}_s + \alpha_s\rho_s\vec{g} + K_{fs}(\vec{u}_f - \vec{u}_s), \tag{3}$$

where $\overline{\overline{\tau}}$ is shear stress tensor, $\vec{g}$ is the gravity acceleration, $p_s$ is the solids pressure and $K_{fs} = K_{sf}$ are the fluid–solid momentum exchange coefficients or two-phase drag coefficients. The particle or solids pressure, $p_s$, is caused by particle interactions (collisions). This pressure transmits a force both by short-duration collisional impacts, as well as by longer-duration particle–particle contact. The particle pressure gradient term serves to keep the particles apart so that the calculated particle volume fraction cannot exceed the maximum concentration attainable for a given size distribution of particles. A value of 0.64 (see Huilin et al., 2001) was assumed

for this maximum particle volume fraction, which is close to the packing limit of a BCC crystal structure (0.68).

The solid pressure, $p_s$, is determined from an equation of state similar to the van der Waals equation of state for fluids, as discussed by Chapman and Cowling (1990) and Gidaspow (1994):

$$p_s = \alpha_s \rho_s \Theta_s + 2\rho_s(1+e_{ss})\alpha_s^2 g_{oss}\Theta_s, \tag{4}$$

where $e_{ss}$ is the coefficient of restitution, $\Theta_s$ is the "granular temperature", and $g_{oss}$ is the radial distribution function. The latter is a correction factor that modifies the probability of collisions between particles when the mixture becomes dense and is obtained by the methods of the Chapman and Cowling (1990) theory of non-uniform gases. The radial distribution function is equal to unity when the particles are loosely packed, and becomes infinite when the particles are so closely packed that relative motion is impossible. The radial distribution function given by Ding and Gidaspow (1990) was used in the current work:

$$g_{oss} = \frac{3}{5}\left[1 - \left(\frac{\alpha_s}{\alpha_{s,max}}\right)^{\frac{1}{3}}\right]^{-1}. \tag{5}$$

Closure of the governing mass and momentum balances is provided by constitutive equations. The stress tensor for both phases is given by the Newtonian stress–strain relation. The solid stress–strain tensor is given by

$$\tau_{s,ij} = \alpha_s\mu_s\left(\frac{\partial u_{s,i}}{\partial x_j} + \frac{\partial u_{s,j}}{\partial x_i}\right) + \left(\alpha_s\lambda_s - \frac{2}{3}\alpha_s\mu_s\right)\delta_{ij}\frac{\partial u_{s,l}}{\partial x_l}, \tag{6}$$

where $\mu_s$ is the solid viscosity, $\lambda_s$ is the solid bulk viscosity and $\delta_{ij}$ is the Kronecker delta.

Non-Newtonian properties of the particulate phase can be taken into account by modeling the particle (solid) viscosity as a function of the fluid volume fraction, as discussed further below.

The solids shear stress tensor contains shear and bulk viscosities arising from particle momentum exchange due to translation and collision. A frictional component of viscosity has been included to account for the viscous-plastic transition that occurs when particles of a solid phase reach the maximum solid volume fraction. Thus, the total solid shear stress is given by

$$\mu_s = \mu_{s,col} + \mu_{s,kin} + \mu_{s,fric} \tag{7}$$

The collisional and kinetic viscosities of the solid phase are given by Syamlal et al. (1993) as

$$\mu_{s,col} = \frac{4}{5}\alpha_s\rho_s d_s g_{oss}(1+e_{ss})\left(\frac{\Theta_s}{\pi}\right)^{1/2}, \tag{8}$$

$$\mu_{s,kin} = \frac{\alpha_s\rho_s d_s\sqrt{\Theta_s\pi}}{6(3-e_{ss})}\left[1 + \frac{2}{5}(1+e_{ss})(3e_{ss}-1)\alpha_s g_{oss}\right], \tag{9}$$

where $d_s$ represents particle diameter. The solids bulk viscosity accounts for the resistance of the granular particles to compression and expansion, and has the following form, according to Lun et al., 1984):

$$\lambda_s = \frac{4}{3}\alpha_s\rho_s d_s g_{oss}(1+e_{ss})\sqrt{\frac{\Theta_s}{\pi}}. \tag{10}$$

Frictional viscosity generation due to friction between particles, and between particles and walls, becomes especially significant as the solids volume fraction approaches the packing limit. The following expression derived by Schaeffer (1987) was used to estimate the frictional viscosity:

$$\mu_{s,fr} = \frac{p_s \sin\phi}{2\sqrt{I_{2D}}}, \tag{11}$$

where $\phi$ is the angle of internal friction, and $I_{2D}$ is the second invariant of the deviatoric stress tensor (see Schaeffer, 1987).

The fluid–solid exchange coefficient used here is given by Syamlal et al. (1993), and is based on the measurement of the terminal velocities of particles in fluidized beds. These correlations give exchange coefficients in terms of the volume fraction and relative Reynolds number as

$$K_{sf} = \frac{3\alpha_s\alpha_f\rho_f}{4u_{rs}^2 d_s} C_D\left(\frac{Re_s}{u_{rs}}\right)|\vec{u}_s - \vec{u}_f| \tag{12}$$

in which the relative Reynolds number is defined as

$$Re_s = \frac{\rho_f d_s|\vec{u}_s - \vec{u}_f|}{\mu_f}. \tag{13}$$

The terminal velocity correlation for the solid phase was obtained experimentally by Garside and Al-Dibouni (1977)

$$u_{rs} = 0.5\left(A - 0.06Re_s + \sqrt{(0.06Re_s)^2 + 0.12Re_s(2B - A) + A^2}\right), \tag{14}$$

where the coefficients of $A$ and $B$ are specified as functions of the liquid volume fraction:

$$\begin{aligned} B &= 0.8\alpha_f^{1.28} \quad \text{for } \alpha_f \leqslant 0.85, \\ B &= \alpha_f^{2.65} \quad \text{for } \alpha_f > 0.85, \\ A &= \alpha_f^{4.14}. \end{aligned} \tag{15}$$

The drag coefficient used was determined by Dalla Valle (1948)

$$C_D = \left(0.63 + \frac{4.8}{\sqrt{Re_s/u_{rs}}}\right)^2. \tag{16}$$

The granular temperature for the solid phase is proportional to the kinetic energy of the random motion of the particles. Ding and Gidaspow (1990) derived a transport equation from kinetic theory that has the form:

$$\frac{3}{2}\left[\frac{\partial}{\partial t}(\rho_s\alpha_s\Theta_s) + \nabla\cdot(\rho_s\alpha_s\vec{u}_s\Theta_s)\right] = -(p_s\bar{\bar{I}} + \bar{\bar{\tau}}_s) : \nabla\vec{u}_s + \nabla\cdot(k_{\Theta s}\nabla\Theta_s) - \gamma_{\Theta s} + \phi_{sf} \tag{17}$$

where $-(p_s\bar{\bar{I}} + \bar{\bar{\tau}}_s) : \nabla\vec{u}_s$ is the generation of energy by the solid stress tensor, $\nabla\cdot(k_{\Theta_s}\nabla\Theta_s)$ is the diffusion of energy, with $k_{\Theta_s}$ as diffusion coefficient, $\gamma_{\Theta_s}$ is the collisional dissipation of energy, $\phi_{sf}$ is the energy exchange between fluid and solid phase.

The rate of energy dissipation within the solid phase due to interparticle collisions, as derived by Lun et al. (1984), is given by

$$\gamma_{\Theta_s} = \frac{12(1 - e_{ss}^2)g_{0,ss}}{d_s\sqrt{\pi}}\rho_s\alpha_s^2\Theta_s^{3/2}. \tag{18}$$

Transfer of the kinetic energy of random fluctuations in particle velocity from the solid phase to the fluid phase is represented by the expression derived by Gidaspow et al. (1992) as

$$\phi_{fs} = -3K_{fs}\Theta_s \tag{19}$$

### 2.2. Solution procedure

The governing set of partial differential equations was discretized using a finite volume technique, as given by Patankar (1983). The discretized equations along with the initial and boundary conditions were solved using FLUENT™. The conservation equations were integrated using power law differencing in space, and implicit differencing in time, in such a manner that the integral conservation is satisfied over the calculation domain, over a time interval. Discretization of the convection terms using a power law interpolation scheme provides formal local accuracy between first and second order (see Patankar, 1983). The power law scheme provides a better approximation to the exact solution of steady one-dimensional convection and diffusion

equations and has been adopted for three-dimensional problems. It is more robust and less computationally intensive than higher order schemes, and provides an extremely good representation of the exponential behavior of the exact solution of one-dimensional convection–diffusion equations (see Patankar, 1983). The SIMPLE algorithm (Patankar, 1983) was used to relate the velocity and pressure corrections and to reformulate the continuity equation in terms of a pressure correction equation. The set of linearized algebraic equations was solved using a tridiagonal matrix algorithm.

The system simulated was a rectangular spouted vessel with a central draft duct (cf. Fig. 2, and description below) that was constructed to provide validation data for the simulations. In order to reduce computational time, only one quadrant of the rectangular vessel, as defined by its two vertical planes of symmetry, was modeled. This computational domain was divided into a finite number of non-overlapping control volumes, each surrounding a grid point. Scalar variables such as pressure, phase volume fractions, and turbulence properties were stored at the grid points. A staggered grid arrangement was used, and the velocity components were stored in the control volume surfaces (see Patankar, 1983). The entire computational domain was represented with a set of computational control volumes consisting of 2288 structured cells; i.e., $(22, 26, 4)$ sections in the $(x, y, z)$ directions, with corresponding physical dimensions (to the rectangular spouted vessel) of $(0.12, 0.36, 0.0127)$ m. A grid independence study was performed in previous work (Shirvanian et al., 2001) that indicated this domain size was adequate to capture the physical behavior of the system.

The boundary conditions include the two planes of symmetry since only one quadrant of the physical domain was simulated. The inlet liquid velocity and the outlet pressure (1 atm) were specified. ''No-slip'' boundary conditions were assumed at the walls for the liquid phase. Interactions of particles with the walls were modeled with the same formulation used for solids pressure and granular viscosity for the particle–particle interactions, except that the walls were conceptually treated as very ''large'' particles. Therefore, in the solid phase the particles can move tangentially while in contact with the wall; i.e., they can exhibit some ''slip'' as determined by wall friction (which was assumed to be the same as between particles).

The solids volume fraction in a domain of known volume was specified at the beginning of each simulation to correspond to the desired solids loading (defined as the total mass of particles in the bed). The particles used in the simulation were monodisperse glass spheres with a density of 2540 kg/m$^3$. Values of the coefficient of restitution and the friction coefficient for these particles were assumed to be 0.97 and 0.092, respectively, according to the measurements of Foerster et al. (1994) for soda lime glass spheres. The same coefficient of

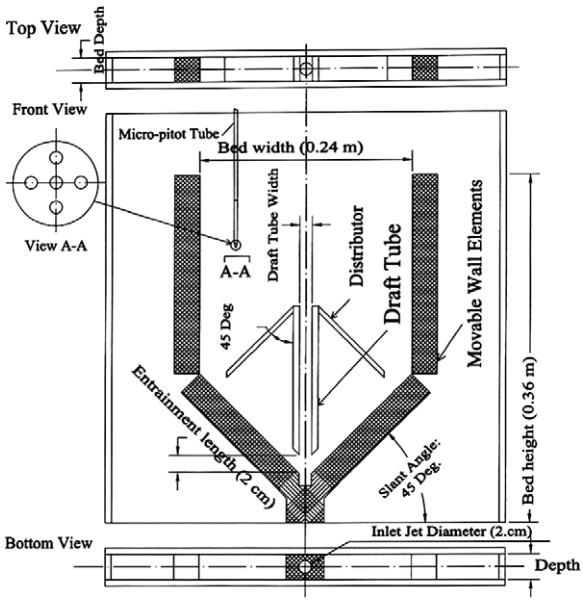


Fig. 2. Rectangular slot, spouted vessel for hydrodynamics investigations.

friction was also assumed for interactions between the walls and the particles. The liquid phase was water at 25 °C. In addition to the preceding values, the "standard" set of parameter values was defined to include an inlet jet velocity of 0.8 m/s, corresponding to 0.252 l $s^{-1}$ (4 gpm), and 200 g of 1 mm diameter glass particles.

Zero velocity initial conditions were used for both the liquid and solid phases everywhere in the computational domain. In order to improve convergence and save computational time, computations were initiated by assuming laminar flow for both the fluid and solid phases, and allowing the flows to develop up until 3 s in real time. The resultant "laminar flow" solution at 3 s was then used as an "initial condition" for the remainder of the simulation that assumed turbulent solid and liquid phase flow until steady-state conditions were attained (at approximately 10 s for the "standard" case). A $k$–$\varepsilon$ turbulence model was used for both the solid and liquid phases (e.g., see Fan and Zhu, 1998).

The time step selected for the simulations was 0.001 s. Simulation of a total real time of 20 s required between 24 and 72 h to run on Pentium III computers, depending on the solids loading.

### 2.3. Model validation

Simulation results were compared to experimental data obtained in a rectangular spouted vessel apparatus in order to validate model results. The experimental results are reported in more detail elsewhere (Shirvanian and Calo, submitted for publication). A summary of the experimental approach is provided below for the current purposes.

The rectangular spouted vessel apparatus shown in Fig. 2, was constructed for experimental hydrodynamic studies. Two 40.6 cm × 40.6 cm × 35.6 cm plexiglass™ sheets served as the front and back of the spouted vessel. The rectangular draft duct and distributor were also made of plexiglass™. A "hot glue gun" was used to attach them to the front and back plates. Hard rubber strips were used to form the sides of the vessel, and to serve as a water seal when clamped between the front and back plates of the spouted vessel.

The feed water for the inlet jet was pumped from a reservoir tank located under the spouted vessel. The water exited the vessel at the top over two overflow weirs that emptied back into the reservoir tank in order to provide continuous circulation.

A micro-pitot tube, constructed by Aeroprobe Corp., was used to measure pressure and the three velocity components throughout the spouted vessel. This system consisted of five probes of 0.508 mm (0.02 in.) in diameter, mounted on a conical tip of 0.3175 cm (0.125 in.) in diameter. Each port was connected with flexible Tygon tubing to a pressure transducer, capable of measuring 0–6895 Pa (0–l psi g). The electrical signal from each pressure transducer was fed to a pressure scanner device. In this manner, the five holes in the probe communicated with the five transducers of the scanner. The scanner was interfaced via a laboratory computer through a CIO-DAS08 data acquisition board and signal conditioning software provided by the manufacturer.

An $x$–$z$ translator was used to position the probe at desired coordinate locations. It employed two stepper motors controlled through the GPIB port. The *Aeroacquire* program and calibration data for the sensors supplied by Aeroprobe Corp., were used to resolve the pressure data into velocity vectors. The presence of the 0.3175 cm diameter probe in the 2.54 cm thick vessel was not observed to produce any observable perturbations on the operation/behavior of the spouted vessel.

## 3. Results

### 3.1. Comparisons of simulation results with data

The particle circulation rate (g/s) as a function of solids loading (defined as the total mass of particles in the bed) for the "standard" case (defined above) is presented in Fig. 3(a), along with corresponding experimental data obtained in the apparatus as described above. As shown in this figure, both the simulation results and the data exhibit an asymptotic approach to a constant particle circulation rate with increasing solids loading. We refer to this behavior as "choking." The "critical loading" is the solids loading required to attain 90% of the asymptotic constant value. Thus, for example, the critical loading in Fig. 3(a) is about 100 g. From this figure, it may be concluded that the simulation predicts the particle circulation rate to better than 15% for the

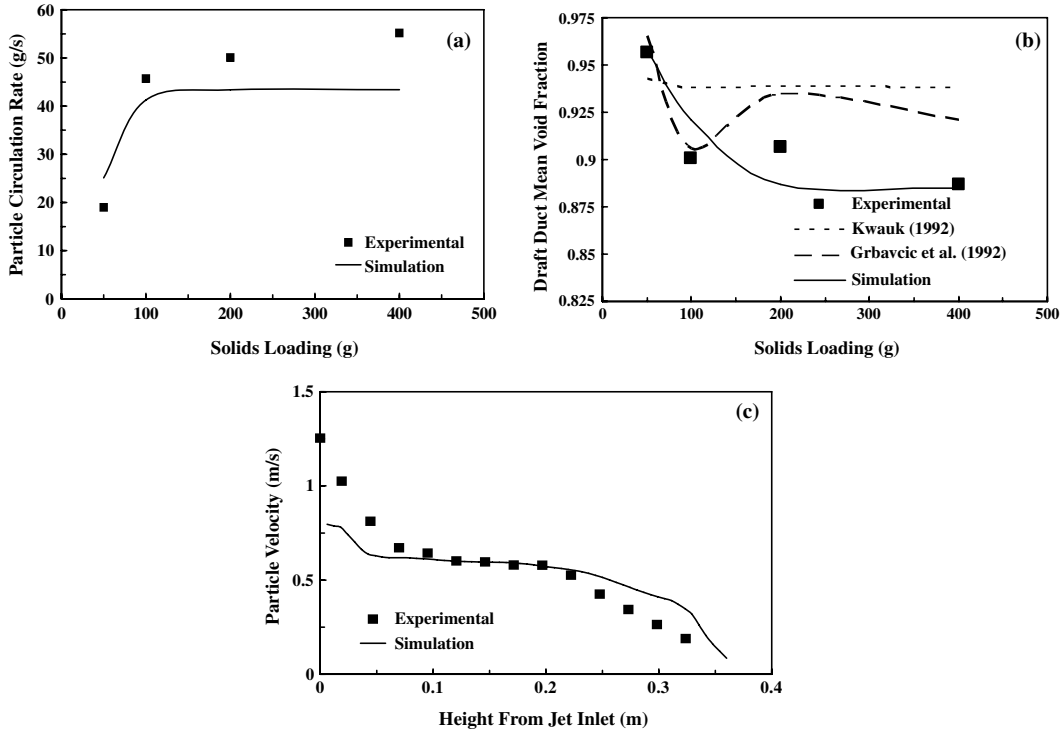


Fig. 3. Comparisons of simulation results with experimental data: (a) particle circulation rate versus solids loading; (b) mean fluid volume fraction in the draft tube versus solids loading (as well as predictions from the correlations of Kwauk (1992) and Grbavcic et al. (1992)); and (c) fluid velocity on the vessel axis. Parameter values: 0.8 m/s inlet fluid velocity; 2 mm glass particles (2540 kg $m^{-3}$); 200 g solids loading (except for (c) which was 50 g); coefficient of restitution and friction coefficient of 0.97 and 0.092, respectively.

experimental conditions examined. Moreover, prediction of the "critical loading" value is seen to be in good agreement with the experimental measurements.

Simulation results for the mean fluid volume fraction in the draft duct for the "standard" case (defined above) are presented in Fig. 3(b), along with the corresponding experimental results, as well as predictions from the semi-empirical correlations of Kwauk (1992) (based on fluid volume fraction distributions obtained in gas–solid risers) and Grbavcic et al. (1992) (based on water-spouted bed data). As shown, there is good agreement between the predicted results from the simulation, our own experimental data, and the two correlations, even that of Kwauk (1992) which is for a much different system. The simulation also correctly predicts that the mean fluid volume fraction remains constant once "critical loading" is attained.

Calculated fluid velocity magnitudes on the axis of the spouted vessel along the lateral plane of symmetry, as a function of height for the "standard" case (defined above) are presented in Fig. 3(c), along with corresponding experimental data. As shown, the agreement is very good except near the bed inlet where the difference between the experimental and simulation results is ~30%. This is attributed to the fluid velocity boundary condition assumed at this location. The inlet geometry of the experimental vessel involves an abrupt transition from a cylindrical feed pipe to an entrainment zone of rectangular cross section. Since there was no simple way to approximate the turbulent ($Re \sim 14\,000$, based on the circular inlet diameter for the "standard" case of 2 cm) velocity profile at the feed pipe exit for this geometry, a uniform velocity profile was assumed. However, the simulation results indicated that the fluid flow field in the entrainment region actually takes on a more "peaked" shape. Thus, the centerline velocity at the jet inlet in the experimental prototype was almost certainly greater than the average velocity value assumed for the flat profile. Application of this correction, if it were to be known or measured in some fashion, would significantly improve the agreement between the simulated and experimental values of the fluid velocity near the vessel inlet.

### 3.2. Simulation results for the "standard" case

The vector velocity fields of the fluid and particle phases, calculated for the "standard" case set of parameter values, are presented in Fig. 4(a) and (b), respectively. Contours of constant particle volume fraction and particle velocity magnitude are also included in these two figures, respectively. As shown, the mechanism for particle entrainment is a pair of fluid vortices located adjacent to the outside wall of the draft duct. The fluid velocity profile (cf. Fig. 4(a)) is peaked in the draft duct, and then flattens progressively with height after it exits the draft duct. The fluid stagnates when it reaches the freeboard, which results in a pressure rise. The particle volume fraction profiles in Fig. 4(a) also show some "mounding" and accumulation of particles on the outside walls of the draft duct near the inlet.

The particle volume fraction contours in Fig. 4(a) show that under these conditions all the particles first fall on the distributor and are then directed to the vessel periphery. Consequently, all the particles spend approximately the same amount of time on the inclined bottom of the vessel. This results in a sharp residence time distribution (RTD) of the particles on the cathode in the actual SBER. This is consistent with experimental data that show the particles remain monodisperse in size even after they have grown considerably due to cumulative metal deposition. Without the distributor, particles tend to enter the moving bed on the cathode at random points along the inclined bottom of the vessel, which would broaden the particle RTD and also the particle size distribution with increasing metal deposition. Thus, the primary function of the particle distributor is to "sharpen" the particle RTD on the cathode. The width of the RTD is almost independent of the hydrodynamics.

As shown in Fig. 4(b), the particle velocity profile in the draft duct is inverted near the draft duct inlet, and then flattens, and eventually becomes peaked in the upper part of the draft duct, more like the fluid velocity at this point, and continues to remain so upon exiting the draft duct. It then broadens and disperses as the particles decelerate and stop in the "fountain" region. The particles then fall downward onto the distributor, where they move centrifugally until they fall onto the inclined bottom at the periphery of the vessel, and then move centripetally along the bottom back towards the entrainment region, completing the particle flow circuit.

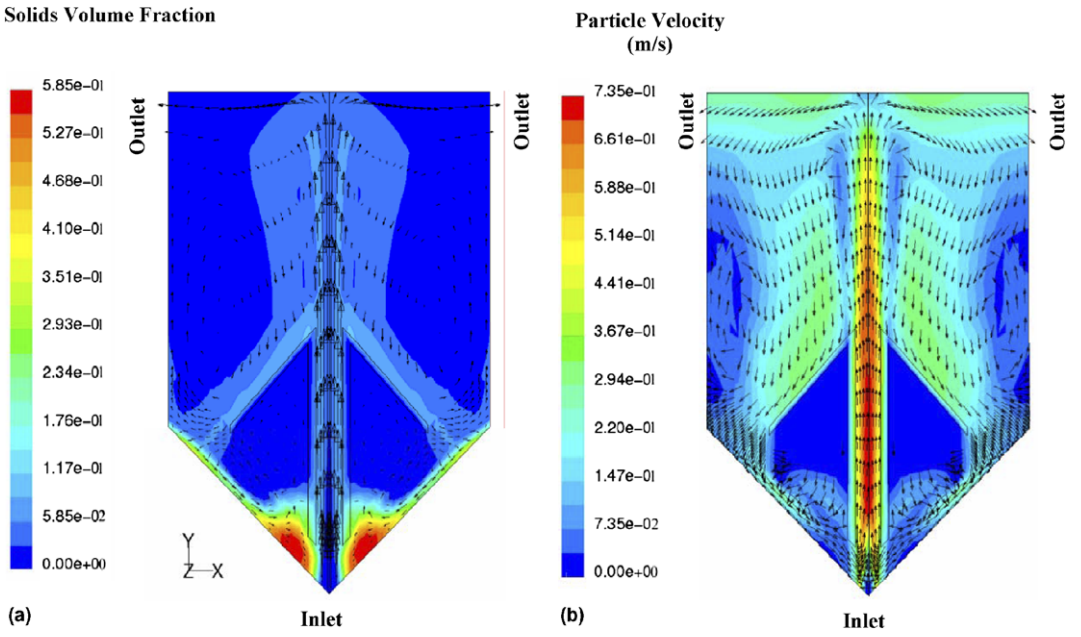


Fig. 4. (a) Solid volume fraction contours superimposed on the fluid vector field for the "standard case", (b) contours of particle velocity magnitude superimposed on the particle vector field (plotted with vectors of constant length for presentation purposes) for the "standard case" set of parameter values: geometry as in Fig. 2; 0.8 m/s inlet velocity; 1 mm glass particles (2540 kg $m^{-3}$); 200 g solids loading; coefficient of restitution and friction coefficient of 0.97 and 0.092, respectively.

The existence of three pairs of counter-rotating vorticies can be seen in the vector field plot in Fig. 4(a) for the liquid phase, and the particle velocity vectors in Fig. 4(b): a large one above the distributor; another in the volume immediately below the distributor; and the pair responsible for particle entrainment at the draft duct inlet. The two pairs immediately above and below the distributor give rise to a stagnation point at the free end of the distributor, with fluid velocities exhibiting opposing directions both above and below it. From this result, it may be inferred that as the particle loading increases (and hence the amount of particles on the distributor) the upward motion of the fluid above the stagnation point acts to retard the flow of particles onto and down the moving bed on the inclined bottom of the vessel, thereby decreasing the particle circulation rate. This is in addition to the particle flow resistance induced by fluid bypassing upwards through the particle moving bed from the entrainment region. The degree of bypassing, and hence the resistance to particle flow on the bottom of the vessel, increases with increasing flow rate. This behavior tends to decrease the particle circulation rate, as borne out by simulations at varying inlet velocities (e.g., see Fig. 7, as discussed below). Therefore, the length of the distributor (or equivalently, the size of the gap between the vessel wall and the end of the distributor) should be optimized such that it does not significantly restrict passage of particles from the distributor downwards to the vessel bottom, and yet be long enough to maintain a sharp particle RTD on the cathode.

### 3.3. Lateral profiles of flow properties in the draft duct

In Fig. 5 are presented lateral profiles on the centerline between the front and back of the vessel for pressure, particle volume fraction, and particle and fluid velocities at three different elevations in the draft duct for the "standard" case under steady-state conditions. The three selected heights are 0.04, 0.1 and 0.19 m above the jet inlet, which correspond to the entrance, middle, and exit of the draft duct. The lateral static pressure

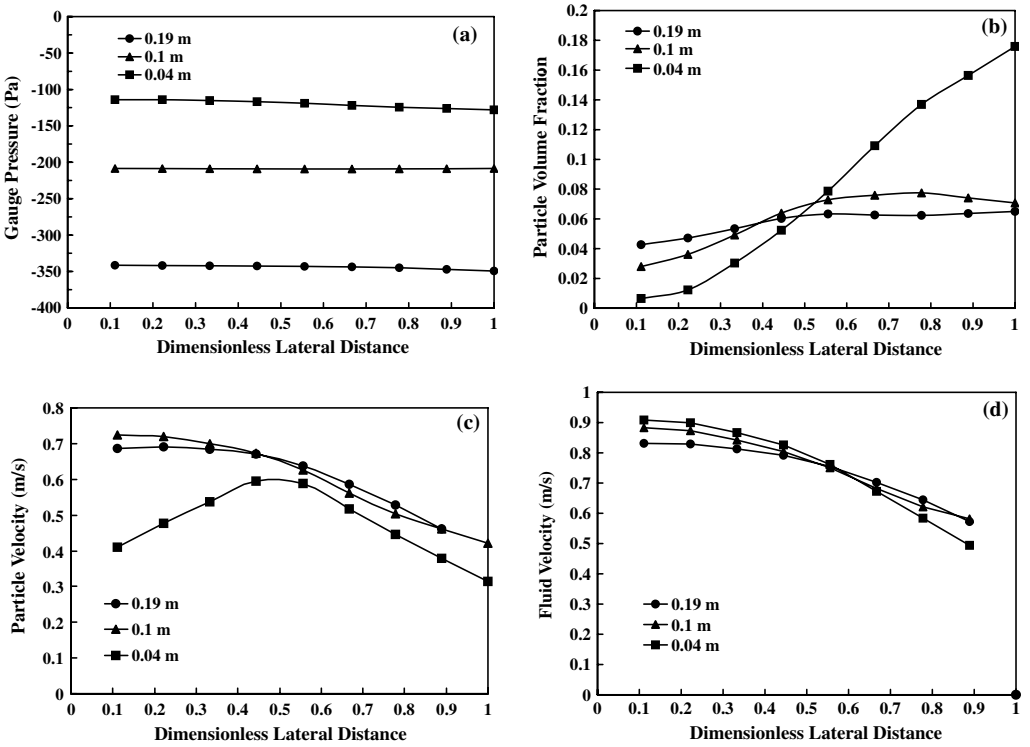


Fig. 5. Lateral profiles in the draft duct of (a) pressure; (b) particle volume fraction; vertical component of the (c) particle velocity; and (d) the liquid velocity, as a function of dimensionless lateral distance from the center axis (0) to the wall (1) at three selected elevations for the "standard case" set of parameter values.

profiles at these three elevations are presented in Fig. 5(a). As shown, the pressure is greatest at the bottom, and decreases in height along the draft duct due to frictional losses. The pressure remains relatively constant across the draft duct.

In Fig. 5(b) it is shown that the particle volume faction decreases from the draft duct wall to the axis at all three elevations. This is most pronounced at the bottom of the draft duct. This behavior agrees with the results of a number of other investigations of similar or related systems. For example, Kwauk (1992) showed experimentally that the radial solids fraction of FCC catalyst particles in a 90 mm diameter riser decreased from the wall to the axis. This was also observed by He et al. (1994a,b) who measured particle velocity and solids concentration in a spouted bed with a fiber optic probe; and also by Samuelsberg and Hjertager (1996) who investigated the flow patterns in a circulating fluidized bed reactor, both numerically and experimentally using laser doppler anemometry (LDA). In both of these latter studies it was also shown that the particle flux in the axial direction decreases from the axis to the walls.

Fig. 5(c) and (d) show only the vertical components of the fluid and the particle velocities in the draft duct, since the other two components were negligibly small (see also Fig. 4(a) and (b)). In Fig. 5(c) it is shown that (except near the bottom of the draft duct) particle velocities are greatest at the center of the draft duct and decrease towards the wall. This is also consistent with other related observations in the literature such as Huilin et al. (2001), Kawaguchi et al. (1998) and He et al. (1994a,b).

The lateral fluid velocity profiles presented in Fig. 5(d) are typical of turbulent flow profiles in closed ducts, with a large gradient near the walls. It is noted that the last calculated fluid velocity value nearest the wall is located at a grid point that is still about 10% of the radial distance away from the wall, and thus the detailed behavior of the fluid velocity as it decreases to zero at the wall is not shown. The computational grid was established and optimized to show the overall flow behavior within the rectangular vessel, while keeping the computational time at a reasonable level. Thus, while detailed information about the behavior of the fluid and the particles within the boundary layer can, in principle, be obtained by increasing the grid density near the wall boundary, this was not one of the current computational objectives of the model.

### 3.4. Parametric studies

In order to obtain a sense of the effects of the principal variables, calculations were performed by varying one parameter at a time from the "standard" case set of parameter values. In this manner, the most important variables and their sensitivities could be identified, and their effects investigated.

The effect of solids loading on the particle circulation rate and the mean fluid volume fraction in the draft duct are presented in Fig. 6. Just as observed in Fig. 3(a) and (b), "choking" of the spout is evident in this figure. That is, as the solids loading increases, the particle circulation rate and mean fluid volume fraction in the draft duct remain constant beyond the "critical loading" of about 500 g determined for the "standard case."

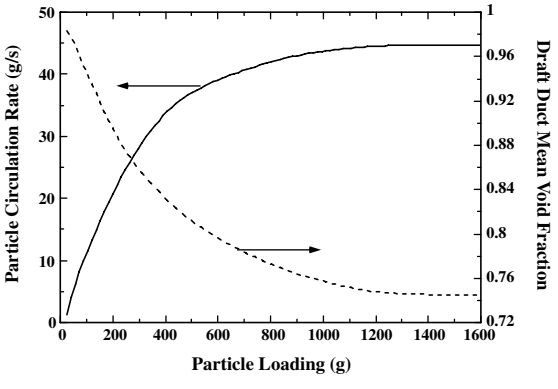


Fig. 6. Effect of solids loading on particle circulation rate and the mean volume fraction in the draft duct for the "standard case" set of parameter values, except for solids loading, which was varied.

In Fig. 7 are presented the effects of inlet fluid velocity on the particle circulation rate and mean fluid volume fraction in the draft duct. As shown in this figure, and as discussed briefly above, the particle circulation rate decreases and the mean fluid volume fraction in the draft duct (generally) increases with increasing inlet fluid velocity. A change in the particle circulation rate is apparent at a fluid velocity of about 0.7 m/s. Below this velocity, the circulation rate decreases monotonically with fluid velocity at a steadily increasing rate. Above this velocity, there appears to be an inflection before the circulation rate begins to decrease at roughly the same rate as prior to this velocity. This change in behavior is also reflected as a "dip" in the fluid volume fraction. This trend wherein fluid volume fraction remains constant in the vicinity of 0.7 m/s is an indication of the onset of "choking" at this particular solids loading. Beyond this point, increasing the fluid velocity causes the particle circulation rate to decrease further. Although the momentum of the inlet jet increases with increasing velocity, the momentum of the bypass fluid, which opposes the particulate flow down the inclined vessel bottom, increases as well, which serves to increase the resistance to particle flow in the moving bed down the inclined bottom, thereby decreasing the particle circulation rate.

The effect of particle density on the particle circulation frequency (# $s^{-1}$) and the mean fluid volume fraction in the draft duct are presented in Fig. 8. As shown, for the glass particles and the "standard case" parameters values used, the particle circulation frequency decreases monotonically with density, while the fluid volume fraction increases monotonically. This is primarily due to the fact that although the drag force remains relatively constant, the particle weight increases with particle density. This results in the pressure drop across the draft duct increasing as well, which decreases the particle volume fraction in the draft duct, and also the

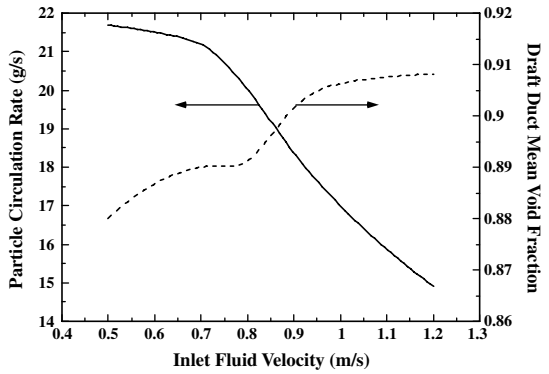


Fig. 7. Effect of inlet fluid velocity on the particle circulation rate and the mean fluid volume fraction in the draft duct for the "standard case" set of parameter values, except for inlet fluid velocity, which was varied.

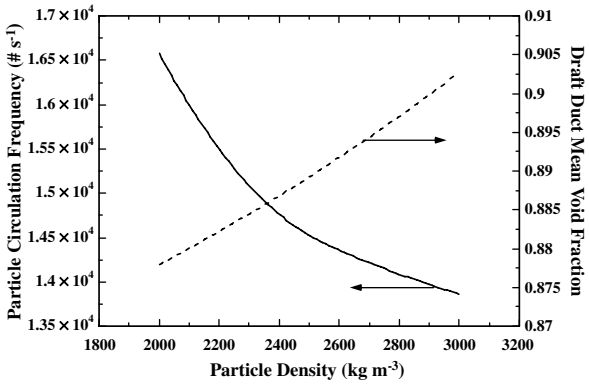


Fig. 8. Effect of solids density on the particle circulation frequency ($s^{-1}$) and the mean void fraction in the draft duct for the "standard case" set of parameter values, except for solids density, which was varied.

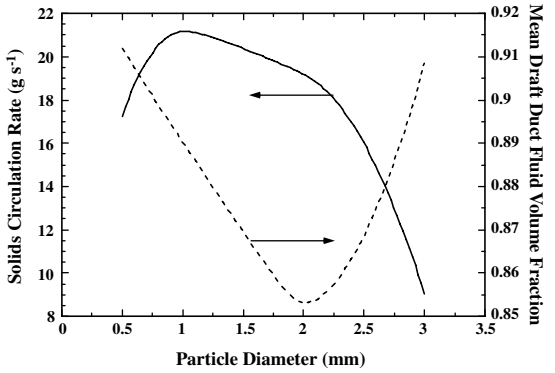


Fig. 9. Effect of particle diameter on the solids circulation rate ($g\,s^{-1}$) and the mean fluid volume fraction in the draft duct for the "standard case" set of parameter values, except for particle diameter, which was varied.

circulation frequency. Thus, it may be concluded that the heavier the particles become, the slower the particle circulation rate, until the bed stops spouting at some critical particle density.

The effects of particle size on the mean fluid volume fraction in the draft duct and the solids circulation rate ($g\,s^{-1}$) are presented in Fig. 9. As shown, the solids circulation rate exhibits a maximum at about 1 mm, while the fluid volume fraction, or, equivalently, the pressure drop across the draft duct, exhibits a minimum at about 2 mm. This behavior can be understood in terms of the drag force on the particles that increases as a function of the diameter squared, and the particle weight that increases as the diameter cubed. Increasing the particle size also increases particle–particle friction, which in turn increases the resistance to particle flow through the entrainment region. As shown in Fig. 9, the net effect is that for smaller glass particles ($d < 1$ mm), increasing drag force with particle size controls the behavior of the particle circulation rate (i.e., it increases); while for larger glass particles ($d > 2$ mm), the combined effect of increasing particle–particle friction and weight begins to control, such that the solids circulation rate decreases and the fluid volume fraction in the draft duct increases with particle size. Particles of intermediate size ($1 < d < 2$ mm) are in a transition regime; i.e., the circulation rate gradually decreases from its maximum, while fluid volume fraction continues to decrease. It is noted, however, that both the total number of particles in the draft duct and the particle circulation frequency (# $s^{-1}$), decrease precipitously and monotonically with increasing particle diameter, exhibiting close to a power law relationship.

## 4. Conclusions

A comprehensive, three-dimensional CFD model has been formulated to quantitatively describe fluid–particle flows in a rectangular spouted vessel. The conservation equations for the solid phase are based on an analogy with the kinetic theory of dense gases, which makes it possible to define a granular temperature and a solid-phase shear viscosity. Model results have been shown to be in reasonably good agreement with our own experimental data (Shirvanian and Calo, submitted for publication), as well as the semi-empirical correlations of Kwauk (1992) and Grbavcic et al. (1992). The model also successfully predicts the phenomenon of "choking" of the particle circulation rate with increasing solids loading.

The mechanism of particle entrainment in the draft duct is shown to be a pair of counter-rotating vortices located at the outside of the draft duct walls near the inlet. The existence of two pairs of counter-rotating vorticies located immediately above and below the particle distributor is also clearly evident in the fluid-phase velocity field vector plots. This behavior creates a stagnation point, with fluid velocities exhibiting opposite directions above and below it, which provides resistance to particle movement from the distributor downwards to the inclined vessel bottom.

The simulations also showed "mounding" of the particles on the outside of the draft duct walls near the inlet at high solids loadings, which would tend to reduce the effectiveness of metal recovery. This condition can be minimized or prevented by reducing the solids loading and operating at lower fluid flow rates to

increase the particle circulation rate and inventory in the draft duct, thereby more fully utilizing the "carrying capacity" of the inlet jet.

This same model has also been used to develop scaling correlations for scale-up/scale-down of rectangular spouted vessels with draft ducts (Shirvanian and Calo, 2004).

## Acknowledgement

This work was supported by a grant from the US Environmental Protection Agency Science to Achieve Results (STAR) program under Grant No. R82-6165.

## References

Chapman, S., Cowling, T.G., 1990. The Mathematical Theory of Non-Uniform Gases, third ed. Cambridge University Press, UK.
Dalla Valle, J.M., 1948. Micromeritics. Pitman.
Ding, J., Gidaspow, D., 1990. A bubbling fluidization model using kinetic theory of granular flow. AIChE J. 36, 523–538.
Drew, D.A., Passman, S.L., 1999. Theory of multicomponent fluids. Appl. Math. Sci. 135.
Drew, D.A., 1983. Mathematical modeling of two-phase flow. Ann. Rev. Fluid Mech. 15, 261–291.
Enwald, H., Peirano, E., Almstedt, A.E., 1996. Eulerian two-phase flow theory applied to fluidization. Int. J. Multiphase Flow 22, 21–66.
Fan, L.S., Zhu, C., 1998. Principles of Gas–Solid Flows. Cambridge University Press.
Foerster, S.F., Louge, M.Y., Chang, H., Allia, K., 1994. Measurements of the collision properties of small spheres. Phys. Fluids 6, 1108–1115.
Garside, J., Al-Dibouni, M.R., 1977. Velocity-voidage relationships for fluidization and sedimentation. IEC Proc. Des. Dev. 16, 206–214.
Gidaspow, D., 1994. Multiphase Flow and Fluidization. Academic Press.
Gidaspow, D., Bezburuah, R., Ding, J., 1992. Hydrodynamics of circulating fluidized beds, kinetic theory approach, fluidization VII. In: Proceedings of 7th Engineering Foundation Conference on Fluidization, pp. 75–82.
Grbavcic, Z.B., Garic, R.V., Vukovic, D.V., Hadzismajlovic, Dz.E., Littman, H., Morgan III, M.H., Jovanovic, S.D.J., 1992. Hydrodynamic modeling of vertical liquid–solids flow. Powder Tech. 72, 183–191.
Hattori, H., Nagal, T., Ojshima, Y., Yoshida, M., Nagata, A., 1998. Solids circulation rate in screen-bottomed spouted bed with draft-tube. J. Chem. Eng. Jpn. 31, 633–635.
He, Y.L., Qin, S.Z., Lim, C.J., Grace, J.R., 1994a. Particle velocity profile and solid flow patterns in spouted beds. Can. J. Chem. Eng. 72, 561–568.
He, Y.L., Lim, C.J., Grace, J.R., Zhu, J.X., 1994b. Measurements of voidage profiles in spouted beds. Can. J. Chem. Eng. 72, 229–235.
Huilin, L., Yonglim, S., Yang, L., Yurong, H., Bouillard, J., 2001. Numerical simulations of hydrodynamic behavior in spouted beds. Trans. Inst. Chem. Eng. 79, 593–599.
Jenkins, J.T., Savage, S.B., 1983. A theory for rapid flow of identical, smooth, nearly elastic spherical particles. J. Fluid Mech. 130, 187–202.
Kalwar, M.I., Raghavan, G.S.V., 1992. Spouting of two-dimensional beds with draft plates. Can. J. Chem. Eng. 70, 887–894.
Kawaguchi, T., Tanaka, T., Tsuji, Y., 1998. Numerical simulation of two-dimensional fluidized beds using the discrete element method. Powder Tech. 96, 129–138.
Kwauk, M., 1992. Fluidization. Science Press, Hong Kong.
Lefroy, G.A., Davidson, J.F., 1969. The mechanics of spouted beds. Trans. Inst. Chem. Eng. 47, T120–T128.
Littman, H., Morgan III, M.H., Vukovic, Dv.V., Zdanski, F.K., Grbavcic, Z.B., 1979. A theory for predicting the maximum spoutable height in a spouted bed. Can. J. Chem. Eng. 57, 684–692.
Lun, C.K.K., Savage, S.B., Jeffrey, D.J., Chepurniy, N., 1984. Kinetic theories for granular flow: Inelastic particles in couette flow and slightly inelastic particles in a general flow field. J. Fluid Mech. 140, 223–256.
Marschall, K.J., Mleczko, L., 1999. CFD modeling of an internally circulating fluidized-bed reactor. Chem. Eng. Sci. 54, 2085–2093.
Mathur, K.B., Epstein, N., 1974. Spouted Beds. Academic Press, New York.
Matthew, M.C., Morgan III, M.H., Littman, H., 1988. Study of the hydrodynamics within a draft tube spouted bed system. Can. J. Chem. Eng. 66, 908–918.
Morgan III, M.H., Day, J.Y., Littman, H., 1985. Spout voidage distribution, stability and particle circulation rates in spouted beds of coarse particles—1. Theory. Chem. Eng. Sci. 40, 1367–1377.
Morgan III, M.H., Littman, H., Sastri, B., 1988. Jet penetration and pressure drop in water spouted beds of fine particles. Can. J. Chem. Eng. 66, 735–739.
Patankar, S.V., 1983. Numerical Heat Transfer and Fluid Flow. Hemisphere, New York.
Samuelsberg, A., Hjertager, B.H., 1996. An experimental and numerical study of flow patterns in a circulating fluidized bed reactor. Int. J. Multiphase Flow 22, 575–591.
Savage, S.B., Jeffrey, D.J., 1981. The stress tensor in a granular flow at high shear rates. J. Fluid Mech. 100, 255–272.
Schaeffer, D.G., 1987. Instability in the evolution equations describing incompressible granular flow. J. Diff. Eq. 66, 19–50.
Shirvanian, P.A., Calo, J.M., 2004. Hydrodynamic scaling of a rectangular spouted vessel with a draft duct. Chem. Eng. J. 103, 29–34.
Shirvanian, P.A., Calo, J.M., 2005. Copper recovery in a particulate spouted bed electrode. J. Appl. Electrochem. 35, 101–111.

Shirvanian, P.A., Calo, J.M., submitted for publication. An experimental investigation of the hydrodynamics of a rectangular spouted vessel with a draft duct. Chem. Eng. J.

Shirvanian, P.A., Calo, J.M., Hradil, G., 2001. An investigation of the hydrodynamics of a rectangular slot, spouted bed. In: Proceedings of 2001 ASME International Mechanical Engineering Congress & Exposition, Session FE-10B, Fluids Engineering Division, NY.

Syamlal, M., Rogers, W., O'Brien, T.J., 1993. MFIX Documentation: vol. 1, Theory Guide. DOE/METC-9411004, NTIS/DE9400087, National Technical Information Service, Springfield, VA.